

THE BLACK HOLE MASS AND THE STELLAR RING IN NGC 3706¹

KAYHAN GÜLTEKIN¹, KARL GEBHARDT², JOHN KORMENDY², TOD R. LAUER³, RALF BENDER⁴, SCOTT TREMAINE⁵, AND DOUGLAS O. RICHSTONE¹

¹Department of Astronomy, University of Michigan, 500 Church Street, Ann Arbor, MI 48109 kayhan@umich.edu.

²Department of Astronomy, University of Texas, 1 University Station C1400, Austin, TX, 78712, USA

³National Optical Astronomy Observatory, P.O. Box 26732, Tucson, AZ, 85726, USA

⁴Universitäts-Sternwarte München, Ludwig-Maximilians-Universität, Scheinerstr. 1, D-81679 München, Germany and

⁵Institute for Advanced Study, Einstein Dr., Princeton, NJ 08540, USA

Accepted by The Astrophysical Journal

ABSTRACT

We determine the mass of the nuclear black hole (M) in NGC 3706, an early type galaxy with a central surface brightness minimum arising from an apparent stellar ring, which is misaligned with respect to the galaxy's major axis at larger radii. We fit new *HST*/STIS and archival data with axisymmetric orbit models to determine M , mass-to-light ratio (Υ_V), and dark matter halo profile. The best-fit model parameters with 1σ uncertainties are $M = (6.0_{-0.9}^{+0.7}) \times 10^8 M_\odot$ and $\Upsilon_V = 6.0 \pm 0.2 M_\odot L_{\odot,V}^{-1}$ at an assumed distance of 46 Mpc. The models are inconsistent with no black hole at a significance of $\Delta\chi^2 = 15.4$ and require a dark matter halo to adequately fit the kinematic data, but the fits are consistent with a large range of plausible dark matter halo parameters. The ring is inconsistent with a population of co-rotating stars on circular orbits, which would produce a narrow line-of-sight velocity distribution (LOSVD). Instead, the ring's LOSVD has a small value of $|V|/\sigma$, the ratio of mean velocity to velocity dispersion. Based on the observed low $|V|/\sigma$, our orbit modeling, and a kinematic decomposition of the ring from the bulge, we conclude that the stellar ring contains stars that orbit in both directions. We consider potential origins for this unique feature, including multiple tidal disruptions of stellar clusters, a change in the gravitational potential from triaxial to axisymmetric, resonant capture and inclining of orbits by a binary black hole, and multiple mergers leading to gas being funneled to the center of the galaxy.

Subject headings: galaxies: individual (NGC 3706) — galaxies: kinematics and dynamics — black hole physics — galaxies:nuclei

1. INTRODUCTION

NGC 3706 is one of eight early-type galaxies identified as having a surface brightness profile with a local minimum at the galaxy's center (Lauer et al. 2002, 2005a). Because of projection effects, a central decrease in surface brightness corresponds to a more prominent decrease in luminosity density. The highest surface brightness in NGC 3706 appears to be associated with an axisymmetric, highly flattened, edge-on ring, which is misaligned from the galaxy's major axis at larger radii by about 42° . The other galaxies with central minima (NGC 4073, NGC 4382, NGC 4406, NGC 6876, A260-BCG, A347-BCG, and A3574-BCG) are consistent with having similar rings, but the interpretation is less clear, in part because the rings in these galaxies are not edge-on. Thus NGC 3706 offers a unique look at this phenomenon.

The most likely interpretation of the central stellar system in NGC 3706 is one called “stellar-torus-added” by Lauer et al. (2002), in which stars are brought in close to the galaxy's center, presumably from a merger and tidal stripping of a dense stellar system (Holley-Bockelmann & Richstone 2000) or else from a merger with a system containing enough gas to form stars in situ (Lauer et al. 2002). The stellar tori may be related to the nuclear stellar disks seen in M31 (NGC 224 Lauer et al. 1993), NGC 4486A (Kormendy et al. 2005), and NGC 4382 (Lauer et al. 2005a; Gültekin et al. 2011a) as well as similar structures seen in several other galaxies (e.g., van den Bosch

et al. 1994; Lauer et al. 1995, 1996; van den Bosch et al. 1998; Scorza & van den Bosch 1998; van den Bosch & Emsellem 1998).

Eccentric disks are thought to require a massive dark object to maintain the aligned semimajor axes (Tremaine 1995). There is, however, no alignment problem in a circular ring, and thus the presence of such a structure does not necessarily imply the existence of a central black hole. Lang et al. (2011) have suggested that the Galactic center may have suffered a recent satellite-galaxy merger analogous to those in the stellar-torus-added scenario.

The presence of an edge-on stellar ring in principle makes measurement of a black hole mass more tractable in the same way that flat galaxy disks make measurements of galactic potentials tractable—there is a unique circular speed at any radius, which is directly related to the gradient of the potential. The black-hole mass measurement would be made easier still if it were a filled-in edge-on disk rather than a ring, since the circular speed could be measured at smaller radii. Knowing the mass of the black hole in any galaxy with an obviously unique stellar feature is also useful for determining the degree to which black holes correlate with their host galaxy properties. For example, if the black hole in NGC 3706 and others like it tended to have much larger or much smaller black holes than similarly sized galaxies without these features, then it would be a hint that the tidal stripping or dissipative merging event that is suspected of producing the ring is not connected to what drives the galaxy-black-hole correlations. What we find below is that the black hole mass is small-to-average compared to the predictions of the M - σ and M - L relations.

¹ Based on observations made with the *Hubble Space Telescope*, obtained at the Space Telescope Science Institute, which is operated by the Association of Universities for Research in Astronomy, Inc., under NASA contract NAS 5-26555. These observations are associated with GO proposal 8687.

Section 2 has a brief description of NGC 3706 plus a description of the observations and data new to this work as well as previously published data that we use in our kinematic modeling. In Section 3 we describe our kinematic modeling and results, including our estimates of the black hole mass, mass-to-light ratio, and dark matter halo properties. We end with a brief discussion of the implications of our results including speculations on the origin of a counter-rotating ring in Section 4. We adopted a distance of 46 Mpc to NGC 3706 based on its recession velocity with respect to the cosmic microwave background and an assumed Hubble constant of $H_0 = 70 \text{ km s}^{-1} \text{ Mpc}^{-1}$ (Lauer et al. 2007). All quantities in this paper are scaled to this distance.

2. OBSERVATIONS OF NGC 3706

NGC 3706 is in Faber et al. (1989) group 242. It is classified as an S0 based on images that show the appearance of diffuse starlight outside of an obvious bulge component. It may not be a true S0 galaxy but only appear so because the extended diffuse starlight may be “Malin shells” resulting from recent merger activity (Malin & Carter 1980; Quinn 1984). It is bulge dominated (type I in the Scorza & Bender 1995 classification according to Scorza et al. 1998). Scorza et al. (1998) find a bulge-to-total ratio of $B/T = 0.94$. The disk component of their fits has a scale length of 2.82 kpc—much smaller than their fitted bulge scale length of 8.89 kpc—and has V magnitude -19.25 . Because the galaxy is bulge dominated, the disk component may not arise from a true disk but merely from deviations from the $r^{1/4}$ surface brightness profile, potentially related to the stellar ring. The disk component derived by Scorza et al. (1998) has an inclination of 67° and is typically 1.5 mag arcsec^2 or more fainter than the bulge; so its existence and properties are sensitive to small deviations from the assumed bulge profile. In any case, the contribution of any such disk to the total luminosity is small and will not affect our interpretation. We adopt a bulge magnitude of $M_V = -22.26$ (Scorza et al. 1998; Lauer et al. 2005b). Without the stellar ring, NGC 3706 appears to have a core surface brightness profile. That is, the surface brightness profile has a form $I(r) \sim r^{-\gamma}$ that transitions from a steep power law with $\gamma \sim 1$ at large radii to a shallow core with $\gamma < 0.3$ (Lauer et al. 1995). The conclusion that NGC 3706 has a core, however, might depend on the model-dependent details of bulge-ring decomposition (Lauer et al. 2005b).

NGC 3706’s stellar ring has a total luminosity of about $1.3 \times 10^8 L_{\odot, V}$. It is seen edge-on with a position angle (PA) of 115° . The ring has a maximum in surface brightness at approximately $0''.13$ from the center. The ring has an inner edge of about $0''.1$ and is detectable to at least $0''.4$ at which point there is not enough contrast to separate it from the rest of the stars in the galaxy. Along its minor axis, the ring is unresolved at *Hubble Space Telescope* (*HST*) resolution. Lauer et al. (2002) argued that the limb brightening, or ansae, seen in the stellar feature at *HST* resolution indicates that it is a ring, i.e., there is a minimum in the stellar density at zero radius, rather than a filled disk.

In order to model the kinematics of the galaxy and detect any central black hole, we need high spatial resolution photometry and spectroscopy of the center of the galaxy plus wide-field photometry and spectroscopy. Because of the high surface brightness and thinness of the ring, it makes for an excellent *HST* target. In the following subsections, we describe the data we used in our kinematic modeling. This includes pre-

viously published Wide Field Planetary Camera 2 (WFPC2) data, archival ground-based spectroscopic data, and previously unpublished Space Telescope Imaging Spectrograph (STIS) data.

2.1. Photometry

Our *HST* photometry comes from Lauer et al. (2002) WFPC2 F555W imaging (GO-6597, PI: D. Richstone), which is the only data set to reveal the stellar ring (Fig. 1). Reduction of the NGC 3706 images is described in detail in Lauer et al. (2002). In brief, the data were taken in a 500 s exposure with a square 2×2 pattern of half-pixel steps to provide Nyquist sampling. The images were combined using the Fourier method of Lauer (1999). The PSF was assembled from observed stars obtained close in time to the imaging observations (Lauer et al. 2002, 2005a). The PSF was deconvolved using 40 iterations of the Lucy–Richardson deconvolution (Lucy 1974; Richardson 1972) prior to the subsequent analysis. The WFPC2 data are useful only out to about $100''$; so we add ground-based data provided by Goudfrooij et al. (1994) and Carollo & Danziger (1994) to extend our radial coverage.

2.2. Spectroscopy

As part of GO-8687 (PI: J. Kormendy), we observed Ca II triplet absorption from NGC 3706 with STIS on *HST*. The spectrograph was operated with the G750M grating for two different positions and slit widths. The STIS $52'' \times 0''.1$ slit was placed directly on the WFPC2-measured location of the stellar ring to a requested PA accuracy of 1° . A second STIS pointing was positioned with the $52'' \times 0''.2$ slit at a PA parallel to the stellar ring but offset perpendicularly by $0''.25$ to the North. Figure 1 contains a diagram of the slit positions.

At the ring position, we obtained 6 exposures at 3 dither positions for a total exposure of 15,174 s. At the offset position we obtained 2 exposures at 2 dither positions for a total exposure of 5,648 s. The STIS CCD has a 1024×1024 pixel format, a readout noise of $\sim 1 e^- \text{ pix}^{-1}$, and a gain of 1.0 without on-chip binning. The wavelength range of the spectra was 8257–8847 Å, with a reciprocal dispersion of 0.554 Å pix^{-1} and a spatial scale of $0''.05071 \text{ pix}^{-1}$ for G750M at 8561 Å.

Our reduction of the STIS data followed the standard pipeline. We extracted raw spectra from the multi-dimensional file and then subtracted a constant fit to the overscan region to determine the bias level. We used our iterative *self-dark* technique (Pinkney et al. 2003) to account for dark current. This technique takes into account the STIS CCD’s warm and hot pixels that change on timescales of roughly a day. Then we flat-field, dark-subtract, and shift the spectra vertically to a common dither, combine, and rotate. We then extract one-dimensional spectra using a bi-weight combination of rows.

We extracted line-of-sight velocity distributions (LOSVDs) from the spectra, which were reduced as described in Gültekin et al. (2009a). We deconvolved the observed galaxy spectrum using a library template made of standard stellar spectra (Gebhardt et al. 2003; Pinkney et al. 2003). Table 1 lists the Gauss-Hermite moments of the extracted velocity profiles; Figures 2 and 3 plot the observed LOSVDs and best-fit model in each bin; and Figure 4 contains a plot of the mean velocity, V , and velocity dispersion, σ , as a function of radius.

The magnitude of the uncertainties in the LOSVD bins and of the uncertainties in the Gauss-Hermite moments is neither uniform nor symmetric. The uncertainties are much larger

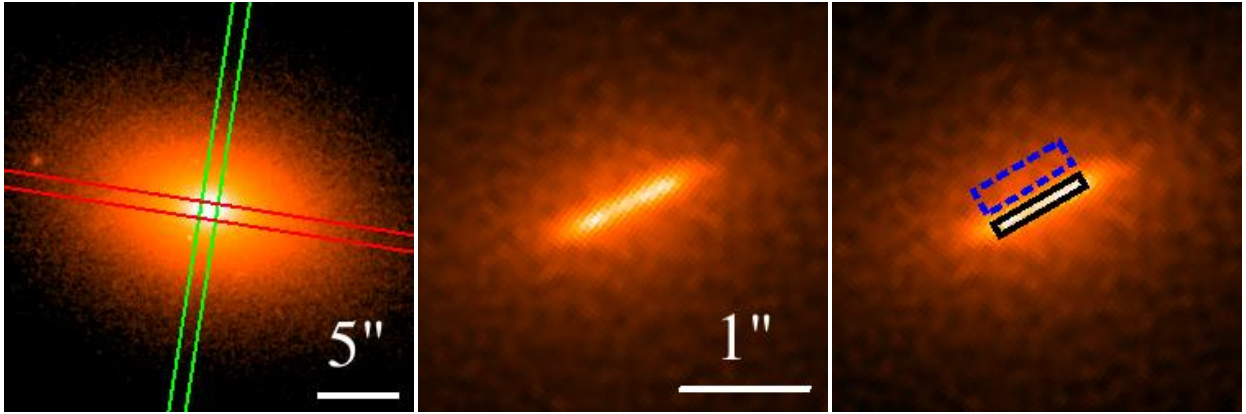


Figure 1. *HST*/WFPC2 F555W images of NGC 3706. The left panel shows the galaxy on large scales with overlays showing the approximate slit positions due to Carollo & Danziger (1994) for the ground-based kinematic data that we use. The center and right panels are from the deconvolution due to Lauer et al. (2002). The center panel shows the presence of the stellar ring and some of the limb brightening. The black and blue boxes in the right panel (at the same scale) show the approximate positions of the STIS slits for the central major axis and off-center major axis pointings, respectively. All images are oriented as north-up, east-left. The scale is shown by the labeled horizontal bar.

for the $R = -0''.075, 0''.25$ spatial bins on the major axis and for the $R = -0''.075$ on the offset slit position. Although the surface brightness is symmetric, the signal-to-noise of the extracted LOSVDs is not symmetric because of changes in the equivalent width of the absorption lines and kinematics. The asymmetry in equivalent width could be a result of an unusual stellar population gradient or non-axisymmetric kinematics, though we find below that our axisymmetric models produce an acceptable fit, and if the gravitational potential is axisymmetric, any asymmetry should rapidly be phase-mixed away.

The velocity profile (Fig. 4) confirms that the stellar feature is a ring rather than a filled disk as the limb brightening indicated (Lauer et al. 2002). The velocity increases from the center towards a maximum of $\sim 100 \text{ km s}^{-1}$ at a projected radius of $R = 0''.075\text{--}0''.1$. If we had observed a disk without a hole in its middle, the velocity dispersion would increase at $R \approx 0$ (assuming there is a black hole at the center), where the circular velocity is highest and the contributions from the two sides of the disk are unresolved. The velocity and dispersion profiles of the STIS data are also plotted in Fig. 5 as a function of distance from the minor axis rather than distance from the center (i.e., cylindrical radial coordinate rather than spherical radial coordinate). This allows one to compare the velocity profile of the putative ring with that of a nearby but offset slit position. Compared to the off-axis velocity profile, the on-axis profile shows rapid rotation, as expected from a ring-like system, but with a large velocity dispersion for its rotational speed ($|V|/\sigma \lesssim 0.3$).

For wide-field kinematics ($R \gtrsim 1''$), we use the velocity and velocity dispersion profiles due to Carollo & Danziger (1994), based on Mg II observations with the ESO 2.2-m telescope. The data were taken along the major and minor axes, *defined by the isophotes at large radii*. The signal-to-noise ratio of these data was limited, so that only the mean velocity and velocity dispersion—not higher moments—were usable. To work with our axisymmetric code, we averaged the data from one side of the galaxy to the other. Despite the low signal-to-noise ratio of the data, these profiles are smooth (Fig. 4) with significant rotation and an increasing dispersion from $\sim 10 \text{ kpc}$ to $\sim 200 \text{ pc}$.

From the ESO spectroscopy, we measured an effective ve-

Table 1
Kinematic Profile for NGC 3706 from STIS Observations

R ($''$)	Bin (pix)	V (km s^{-1})	σ (km s^{-1})	h_3	h_4
-0.250	5	-94 ± 14	360 ± 15	0.087 ± 0.005	-0.060 ± 0.015
-0.075	2	-111 ± 71	264 ± 44	0.035 ± 0.05	-0.036 ± 0.12
0.000	1	30 ± 16	284 ± 15	0.031 ± 0.005	-0.036 ± 0.03
0.075	2	95 ± 10	297 ± 11	0.021 ± 0.001	-0.034 ± 0.023
0.250	5	99 ± 99	258 ± 49	-0.029 ± 0.06	-0.041 ± 0.048
-0.250	5	48 ± 13	311 ± 15	0.052 ± 0.009	-0.025 ± 0.03
-0.075	2	64 ± 86	244 ± 52	0.064 ± 0.028	0.008 ± 0.100
0.000	1	34 ± 69	225 ± 40	-0.014 ± 0.033	-0.041 ± 0.038
0.075	2	-50 ± 9	299 ± 10	0.009 ± 0.004	-0.057 ± 0.022
0.250	5	67 ± 9	282 ± 9	0.011 ± 0.002	-0.037 ± 0.024

Note. — Gauss–Hermite moments for velocity profiles derived from STIS data. Radii are distances from the minor axis, i.e., cylindrical radial coordinate, given in arcsec with negative values indicating the southeast side and positive the northwest side of the slit. The second column gives the width of the radial bin in pixels, which are $0''.05$. The top section gives values for the center positioning with the $0''.1$ slit, and the bottom section gives values for the off-center positioning with the $0''.2$ slit.

locity dispersion of $\sigma_e = 325 \pm 5 \text{ km s}^{-1}$, where

$$\sigma_e^2 \equiv \frac{\int_0^{R_e} [\sigma(r)^2 + V(r)^2] I(r) dr}{\int_0^{R_e} I(r) dr}, \quad (1)$$

where R_e is the effective radius, $I(r)$ is the surface brightness profile, and $V(r)$ and $\sigma(r)$ are the mean velocity and velocity dispersion of the LOSVD, and where the integral is along the major axis. We use the Lauer et al. (2005b) reported value of $R_e = 34''.9$ and integrate equation (1) with cubic spline interpolation and Newton–Cotes quadrature. Other interpolation schemes and quadrature techniques give similar results.

Others (e.g., McConnell et al. 2012) argue that the integral in equation (1) should start not at 0 but at the radius of the black hole’s sphere of influence. There are two potential definitions of the sphere of influence. The first is the classical definition: $R_{\text{infl}} = GM\sigma^{-2}$, where σ , which is generally a function of radius, is evaluated at R_{infl} , a recursive definition that converges quickly. The second is the radius at which the enclosed stellar mass is equal to the black hole mass: $M_*(r < R_{\text{encl}}) = M$. Based on our results below, the classical sphere of influence for NGC 3706 is $R_{\text{infl}} = 25 \text{ pc} \approx 0''.11$, and the enclosed stellar mass radius is $R_{\text{encl}} = 34 \text{ pc} = 0''.15$. Thus for both definitions,

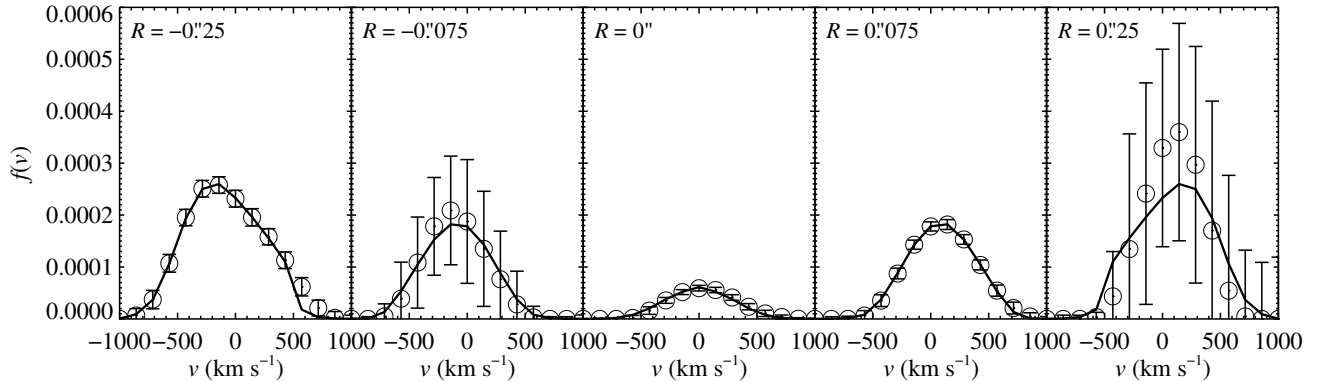


Figure 2. LOSVDs for STIS data from the stellar ring. The circles with error bars are the LOSVD extractions from the STIS data, and the solid line is the best-fit model. Each panel comes from a different spatial bin as indicated in Table 1. The signal-to-noise ratio varies from spatial bin to spatial bin (as discussed in Section 2.2), but is excellent in the first, third, and fourth bin. As the model is axisymmetric, the model LOSVDs at R and $-R$ are mirror images. The y-axis normalization is arbitrary but consistent across all panels of this figure and of Fig. 3 such that the integral of the curves is proportional to the total light in each bin. The differences in the integral of each panel are because of the different numbers of pixels in each radial bin, the different slit widths between this figure and Fig. 3, and the different amount of light.

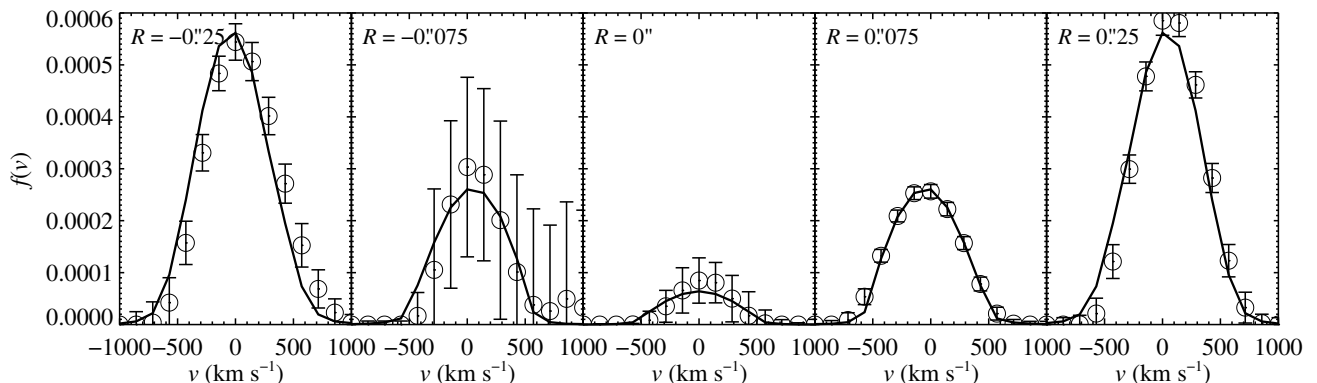


Figure 3. Same as Fig. 2 but for the offset STIS slit position.

we are able to resolve the sphere of influence of the black hole, a fact that can only be determined after the black hole mass has been measured (Gültekin et al. 2011b). Using this alternative definition of σ_e makes only a 1% or 2% difference.

3. MODELING

We use the Schwarzschild (1979) orbit-based method to make axisymmetric three-integral models of NGC 3706 using the implementation described in Gebhardt et al. (2003) and Siopis et al. (2009). For NGC 3706, the presence of the ring requires an approach different from our usual one. We perform a photometric bulge–ring decomposition, deproject each component separately, and then combine the deprojected luminosity densities into a single luminosity density.

3.1. Deprojection to luminosity density

For the deprojection, we created a bulge surface brightness image based on the surface brightness profile of the bulge’s minor axis. To create the two-dimensional image, we used the apparent axis ratio at large radii where there is no ring. Inside $0''.5$, the presence of the ring makes determination of bulge axis ratio impossible. We extrapolated from $r = 0''.5$ to the center, assuming no change in the bulge’s axis ratio. We then subtracted the bulge-only image from the total image, leaving only the ring light.

Deprojection of the bulge light proceeded as usual under the assumption that constant luminosity density contours are coaxial spheroids. Because the stellar ring is edge-on, we

enforce an inclination of $i = 90^\circ$. This prescription results in a core profile for the galaxy.

Deprojection of the ring light assumed that the ring is flat, circular, and edge-on. From the unresolved ring height ($z < 0''.05$), the axis ratio at the inner edge is $z/r < 0.5$ and at the outer edge $z/r < 0.125$. A complication in the modeling is that there is a misalignment of the galaxy bulge isophotes at large radii by about 42° from the ring major axis. The ring major axis has $PA = 115^\circ$ at radii $r \leq 0''.4$, whereas the bulge has $PA = 73^\circ$ at radii $r > 6''$ (Fig. 1). The change in PA, or isophotal twist, occurs sharply between semimajor axes of 1 and $2''$ (Lauer et al. 2002). In our model we simply combine the luminosity densities of the two components as if they were coaxial.

A frequent cause of isophotal twists is the projection of a triaxial light distribution, but in this case it is more likely that the change in PA represents the transition from an outer axisymmetric light distribution to an inner distribution, dominated by the ring light, that is axisymmetric relative to a different axis.

3.2. Orientation of data and model

The ground-based spectra come from slits positioned on the galaxy’s major and minor axes at large radii, as is appropriate since these data are used to constrain the large-scale kinematics. In our modeling of the galaxy, we calculate LOSVDs at the central bins of the ground-based slits as if the ring were coaxial with the galaxy bulge. This cannot have any effect because any differences between our model and how the galaxy actually

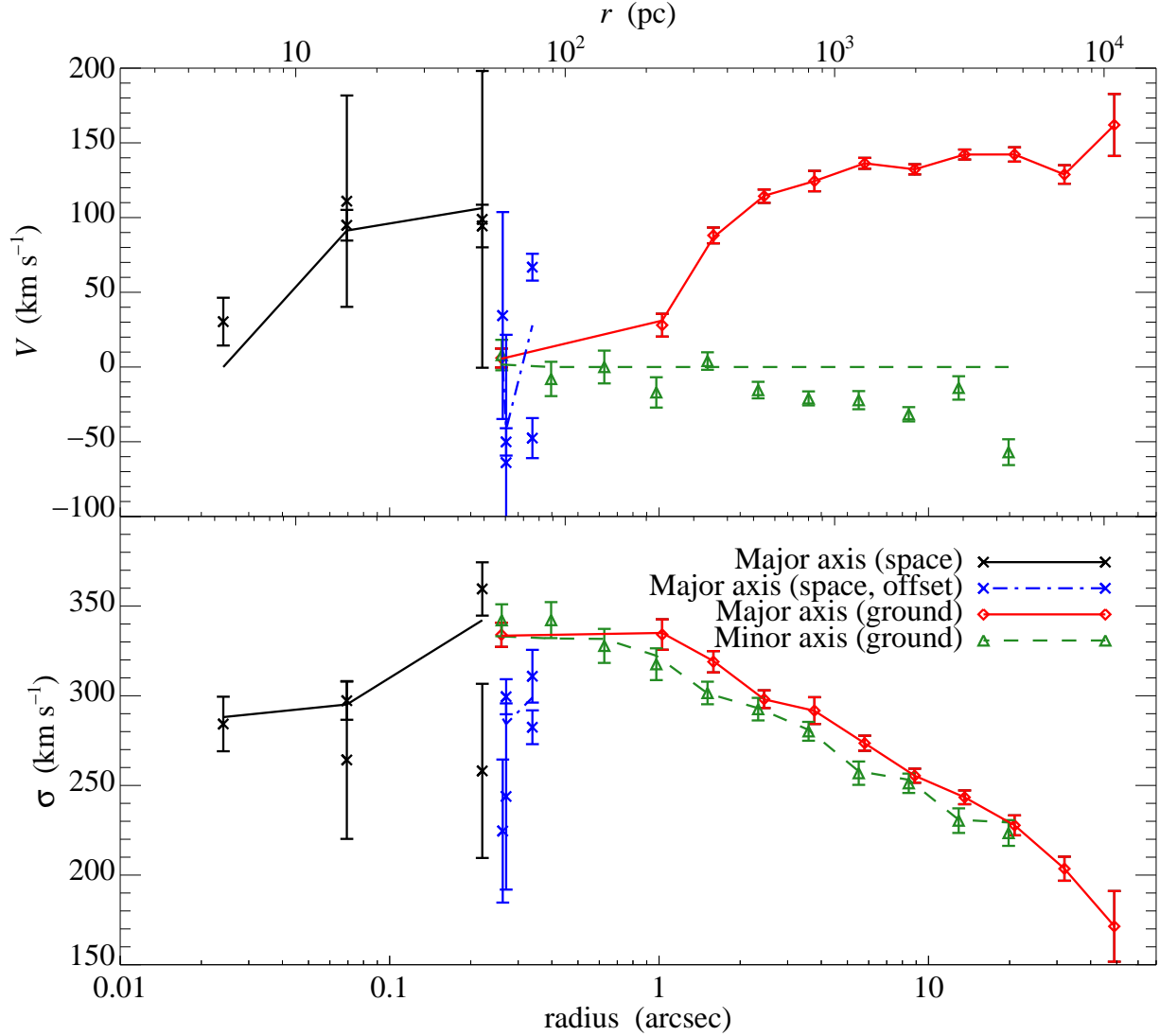


Figure 4. Mean line-of-sight velocity and velocity dispersion of NGC 3706 as a function of radius. Symbols are the data, and lines are the from the best fit model (parameters: $M = 6.0 \times 10^8 M_{\odot}$, $Y_V = 6.0 M_{\odot} L_{\odot, V}^{-1}$, $V_c = 600 \text{ km s}^{-1}$, and $r_c = 30 \text{ kpc}$). Black crosses are STIS major axis; blue crosses are STIS major axis offset by $0''.3$ perpendicular to the slit PA; red diamonds are ESO major axis (due to Carollo & Danziger 1994); and green triangles are ESO minor axis data. Black solid is major axis; blue dot-dashed is offset major axis; red solid is major axis at ground resolution; and green dashed is minor axis at ground resolution. The colors correspond to the slits in Figure 1. Data and models with $r = 0$ are plotted at $r = 0''.025$ on the logarithmic plot. Note that for the STIS data, there are two data points for each radius $r > 0''.025$ and slit position. This is because velocity profiles from each side of the galaxy center were extracted independently. The model, however, is axisymmetric. The ESO data from each side of the galaxy, by contrast, were averaged.

appears are beneath the resolution limit of the ground spectra.

It is possible that the misalignment between our assumed axis of symmetry and the actual axis of symmetry of the outer regions of the galaxy could affect our inference of the stellar mass-to-light ratio. Because of the covariance between black hole mass and stellar mass-to-light-ratio, this could result in incorrect inferences of black hole mass. This also is unlikely to have made a large difference. The mass-to-light ratio that we find best describes the data under our assumptions is entirely reasonable for a galaxy of this size and close to the value obtained by Carollo & Danziger (1994). Finally, if the stellar ring is kinematically decoupled from the rest of the galaxy, as seems reasonable, then modeling the galaxy as having a coaxial stellar ring should not produce substantially different kinematics. The known deviations from our assumptions about

the light distribution, however, are unquantifiable systematic errors that are not reflected in our quoted uncertainties.

3.3. Model parameters

Assuming constant but unknown stellar mass-to-light ratio Y_V , and assuming that the ring and the rest of the galaxy have the same mass-to-light ratio, we generate a stellar mass density, $\rho(r, \theta)$. To this we add a point mass of unknown mass, M , at the center of the galaxy and a dark matter halo potential, parametrized as a spherical cored logarithmic halo with mass density profile

$$\rho(r) = \frac{V_c^2}{4\pi G} \frac{3r_c^2 + r^2}{(r_c^2 + r^2)^2}, \quad (2)$$

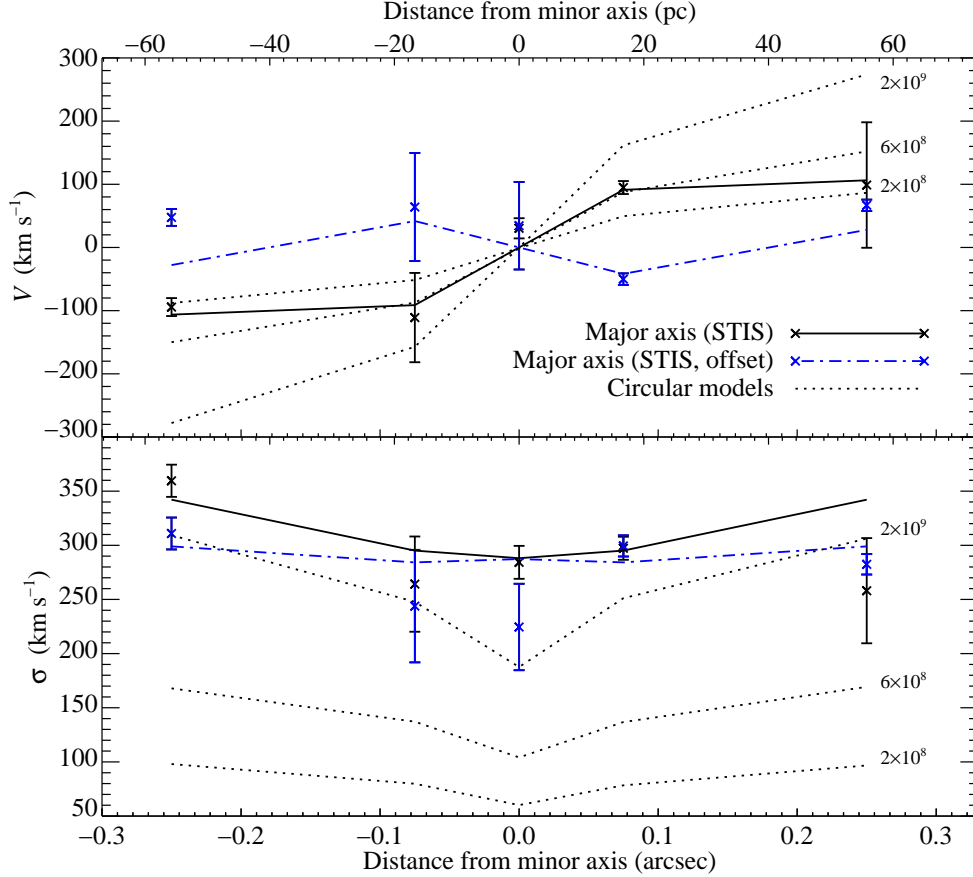


Figure 5. Mean velocity and velocity dispersion profiles (symbols) with best-fit models (lines) for two slit positions: on the major axis (black symbols and black solid line) and parallel to the major axis offset perpendicularly by $0''.3$ (blue symbols and blue dot-dashed line). The abscissa is distance from minor axis, i.e., cylindrical radial coordinate. The much faster rotation speed seen in the on-axis slit is consistent with a rapidly rotating, thin ring of stars. The dotted black lines are results from our simple circular-orbit models (Sect. 4.2) with black hole masses indicated by the numbers at the right of each line and should be compared to the on-axis data. The low value of $|V|/\sigma \lesssim 0.3$ for the stellar ring cannot be explained with a single population of co-rotating stars in circular orbits.

with unknown asymptotic circular velocity, V_c , and core radius, r_c . Each unknown, Υ_V , M , V_c , and r_c becomes a parameter of our model. We calculate orbits of representative stars in the combined potential of the stars, black hole, and dark matter halo, keeping track of the orbit's contribution to the galaxy's surface brightness and line-of-sight-velocity distributions (LOSVDs) in each bin where we have data. The number of orbits is different for each set of parameters but ranged from $\sim 12,000$ – $17,000$ with $\sim 15,000$ a typical value. We calculate the set of non-negative weights of the orbits that minimizes the difference between the LOSVDs of the model and the data, subject to the constraint of matching the surface brightness throughout the galaxy. This brief description of our kinematic modeling necessarily simplifies many of the details, which are expanded in Gebhardt et al. (2003), Gebhardt et al. (2000b), Richstone et al. (2004), Thomas et al. (2004), Thomas et al. (2005), and Siopis et al. (2009). Similar models are described by others (Richstone & Tremaine 1984; Rix et al. 1997; Cretton et al. 1999; Valluri et al. 2004; van den Bosch et al. 2008).

To determine what range of parameters to use, we ran an initial coarse grid in the 4-dimensional parameter space and then used a refined, uniform grid around the best models from the coarse grid. The final range in parameters was $\Upsilon_V = 3$ – $9 M_\odot L_{\odot,V}^{-1}$; $M = 0$ – $2.2 \times 10^9 M_\odot$; $V_c = 100$ – 600 km s^{-1} ; and

$r_c = 5$ – 50 kpc . We also ran models with no dark matter halo, parametrized as $V_c = 0.01 \text{ km s}^{-1}$ and $r_c = 1000 \text{ kpc}$. The gridding of the parameters can be ascertained from Figure 6.

3.4. Modeling results

The best-fit model has parameters $M = 6 \times 10^8 M_\odot$, $\Upsilon_V = 6.0 M_\odot L_{\odot,V}^{-1}$, $V_c = 600 \text{ km s}^{-1}$, and $r_c = 30 \text{ kpc}$. Models with $M = 0$ were ruled out at very high significance, $\Delta\chi^2 = 15.4$. Marginalizing over the other parameters, the 1, 2, and 3σ uncertainty ranges for M are 5.1 – 6.7×10^8 , 3.2 – 8.9×10^8 , and 1.4 – $12 \times 10^8 M_\odot$, respectively. The corresponding uncertainty ranges for Υ_V are 5.8 – 6.2 , 5.3 – 6.6 , and 4.7 – $7.0 M_\odot L_{\odot,V}^{-1}$, respectively. Models without a dark matter halo are ruled out at a significance of $\Delta\chi^2 > 64$, but we cannot disentangle the strong correlation between r_c and V_c to constrain these parameters individually. This is to be expected without good coverage at large radii (e.g., Murphy et al. 2011). We can, however, put weak limits on the central density, i.e., $\rho_c \equiv 3V_c^2/4\pi Gr_c^2$. The best fit value is $\rho_c = 0.02 M_\odot \text{ pc}^{-3}$ with 1, 2, and 3σ uncertainty ranges of 0.016 – 0.04 , 0.005 – 0.12 , and 0.004 – $0.4 M_\odot \text{ pc}^{-3}$. It is worth noting that our best-fit value for V_c is at the maximum value considered for this parameter. Given that there is no sign of convergence, that there is a degeneracy between V_c and r_c , and that we do not have strong data at large

data where we would best be able to get information about the dark matter halo, we did not spend more computational time to find the global minimum of V_c . Our results suggest that as long as some plausible dark matter halo is included in our models, our inferences about the black hole mass and stellar mass-to-light velocity are not strongly affected, even if we cannot constrain the parameters of the dark matter halo.

The projection of χ^2 versus M and versus Υ (Fig. 6) reveals the importance of including a dark matter halo in the mass model. First, we note that for NGC 3706, the models without a dark matter halo (shown as red diamonds in the figure) still rule out the absence of a black hole at high significance, and the mass is consistent with the dark matter halo models at about the 2.5σ level. The best fitting models without a dark halo have higher Υ_V values in order to account for the larger amount of mass at large radii. Since there is a small covariance between Υ_V and M , this results in a smaller black hole mass. The difference between the inferred black hole masses when including and not including a dark matter halo are smaller when the black hole’s gravitational sphere of influence is well resolved, a condition that minimizes the degeneracy (Gebhardt & Thomas 2009; Schulze & Gebhardt 2011; Gebhardt et al. 2011; Rusli et al. 2013).

4. DISCUSSION AND CONCLUSIONS

4.1. *The mass of the black hole*

The mass of the black hole can be predicted from the velocity dispersion of its host galaxy (the $M-\sigma$ relation; Gebhardt et al. 2000a; Ferrarese & Merritt 2000; Tremaine et al. 2002; Gültekin et al. 2009b; McConnell & Ma 2013; Kormendy & Ho 2013) or its host (classical) bulge luminosity (the $M-L$ relation; Kormendy 1993; Kormendy & Richstone 1995; Magorrian et al. 1998; Kormendy & Gebhardt 2001; Häring & Rix 2004; Gültekin et al. 2009b; Kormendy et al. 2011; Sani et al. 2011; McConnell & Ma 2013; Kormendy & Ho 2013).

The effective velocity dispersion we measured in Section 2.2 is $\sigma_e = 325 \text{ km s}^{-1}$. The $M-\sigma$ relation for ellipticals and classical bulges due to Kormendy & Ho (2013) predicts a black hole mass and 68% distribution interval of $M = 2.6^{+2.5}_{-1.3} \times 10^9 M_\odot$. Our best fit mass estimate for the black hole in NGC 3706 is 4.3 times smaller than the $M-\sigma$ relation predicts, or about a 2.2σ outlier compared to the 0.29 dex rms intrinsic scatter. If we exclude the inner 0.4 or $1''$ from the integrals in Equation (1) to avoid possible contamination by the ring, then σ_e reduces to 318 or 300 km s^{-1} , respectively, which would put NGC 3706 closer to the ridge line relation, enough to make it only a 1.7σ low outlier. A dispersion of 300 km s^{-1} also brings makes it less of an outlier from the (Faber & Jackson 1976, i.e., $L-\sigma$) relation for either a core or coreless elliptical (Kormendy & Bender 2013).

The bulge absolute magnitude of NGC 3706 is $M_V = -22.26$. A typical $V-K$ color for a galaxy of NGC 3706’s luminosity is $V-K = +2.98$ (Kormendy & Ho 2013) so that $M_K = -25.24$. At this bulge luminosity, the Kormendy & Ho (2013) $M-L$ relation for ellipticals and classical bulges predicts $M = 1.7^{+1.7}_{-0.9} \times 10^9 M_\odot$. The black hole in NGC 3706 is about 2.9 times smaller, or a 1.5σ outlier for the 0.30 dex rms scatter.

The scaling relations of Kormendy & Ho (2013) make larger predictions for black hole mass than earlier scaling relations (e.g., Tremaine et al. 2002; Gültekin et al. 2009b). The difference in predictions arises mostly from the different intercepts of the relations; the slopes are very similar. The primary rea-

sons for the difference in intercepts are the upward revisions in black hole masses for several sources, the larger number of core ellipticals with large black hole masses, and the rejection of some black hole mass measurements from emission-line rotation curve techniques of poor quality. Other differences are that Kormendy & Ho (2013) did not include galaxies with only upper limits to the black hole mass, and excluded pseudobulges, late-type galaxies, “monster black holes,” and recent mergers, on the grounds that the galaxies are physically very different from the galaxies comprising the bulk of the sample. If, despite the strong arguments in Kormendy & Ho (2013), we include the pseudobulges, late-type galaxies, “monster black holes,” and recent mergers and re-fit the $M-\sigma$ and $M-L$ relations, the new fits to the resulting larger, more diverse sample do not significantly alter the slope or intercept, but they do increase the intrinsic scatter to 0.46 and 0.68 dex for the $M-\sigma$ and $M-L$ relations, respectively. NGC 3706 is still below these forms of the relations, but only by 1.4 and 0.7σ for the $M-\sigma$ and $M-L$ relations, respectively.

NGC 3706’s diffuse starlight extending beyond the well defined bulge, which may be Malin shells, and nuclear stellar ring are both plausibly—but not conclusively—attributed to merger activity. The stellar ring could last for a Hubble time and therefore be a remnant of an earlier merger before a more recent event that resulted in the Malin shells. Several other galaxies that are classified as “mergers in progress” by Kormendy & Ho (2013) also fall below (or to the right of) the scaling relations, especially the $M-L$ relation. Thus, it is not without precedent to find such a small black hole in a host galaxy of this size. Without deep images, however, it is difficult to be certain whether NGC 3706 is a “merger in progress” as defined by Kormendy & Ho (2013). NGC 3706 does differ from other mergers in progress in that it is just as much an outlier in the $M-\sigma$ relation as it is in the $M-L$ relation, whereas the other mergers in progress are closer to the $M-\sigma$ ridge line than they are to the $M-L$ ridge line. Finally we note that the case for NGC 3706 as a merger in progress is far more circumstantial than for the other galaxies identified as such in Kormendy & Ho (2013) and that any merging activity in NGC 3706 could have happened as long as 10^9 yr ago. In any case, as it is only a $\sim 2\sigma$ outlier from the scaling relations, the deviations may not be physically meaningful.

4.2. *The kinematics of the ring*

We did not explicitly constrain our model to use a ring, only that it reproduce (1) the deprojected light distribution, which includes what appears to be a stellar ring, and (2) the observed line-of-sight velocities. Nonetheless, the best orbit models were those that included orbits constituting a stellar ring. Fig. 7 plots the kinematics of the best fitting model in the equatorial plane. At the range of radii marked by shading in the figure ($0''.1 \lesssim r \lesssim 0''.4$), the ring should dominate the light-weighted kinematics. In this range there is a marked decrease in dispersion in the radial and altitude angle directions (drops in σ_r and σ_θ). This is exactly as expected for a stellar ring.

We also fitted the major-axis STIS kinematics with a simple model in which the ring is composed of stars on circular orbits, all traveling in the same direction, conforming to the observed surface brightness in the potential of a central point mass and a reasonable “background” potential. The low value of $|V|/\sigma$ in the ring, however, is inconsistent with such models. The rotation profile can be matched with a central mass much smaller than found by our Schwarzschild modeling, and the dispersion profile can be matched by a much larger mass,

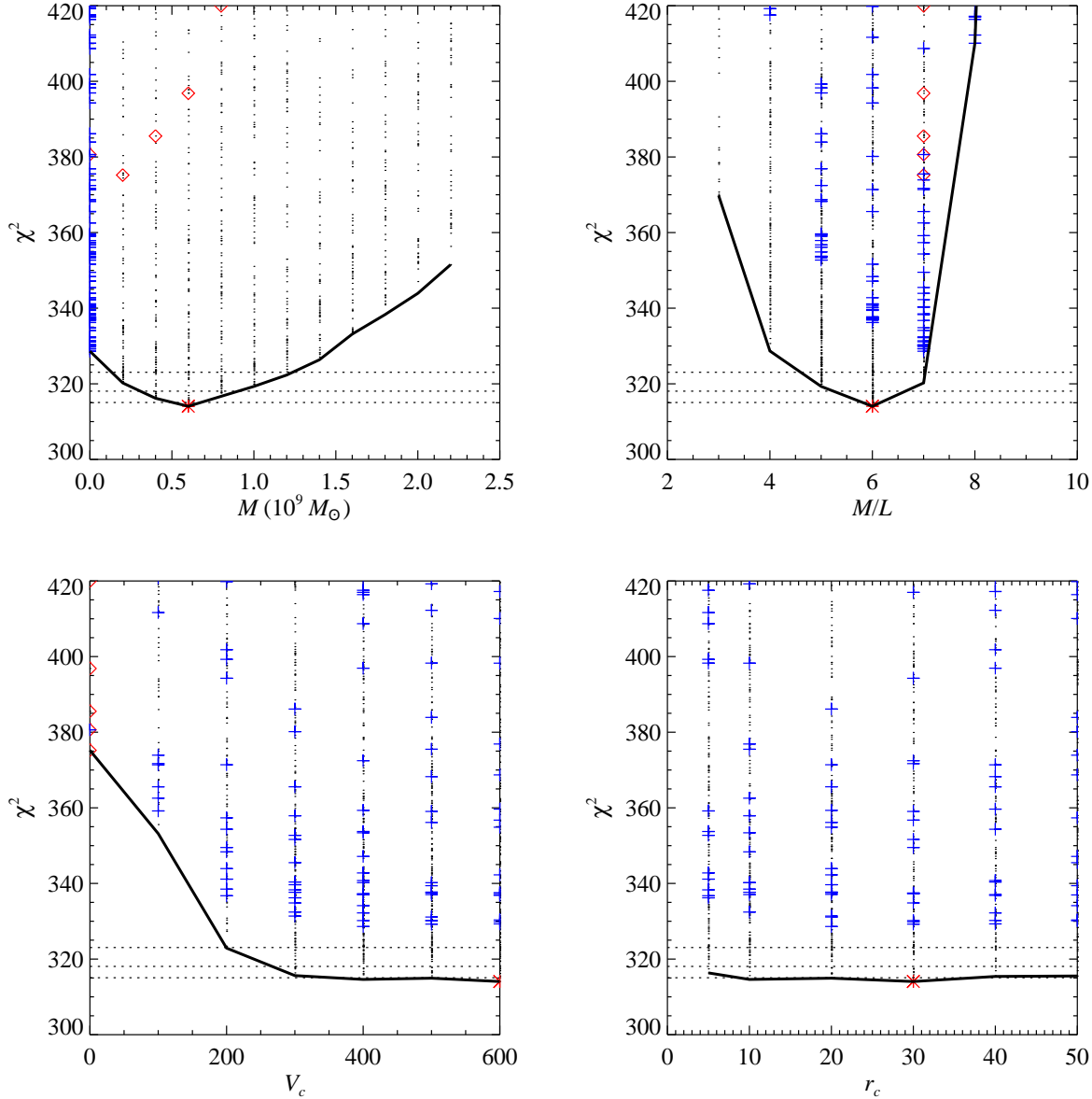


Figure 6. Best-fit models. Each panel plots χ^2 for all models as a function of the given parameter (M , Y_V , V_c , and r_c), projecting through the other three dimensions. All models are plotted as black dots. The best-fit model ($M = 6.0 \times 10^8 M_\odot$, $Y_V = 6.0$, $V_c = 600 \text{ km s}^{-1}$, and $r_c = 30 \text{ kpc}$) is shown with a red asterisk. Models with $M = 0$ are over-plotted with blue crosses, and models with no dark matter halo ($V_c = 0.01 \text{ km s}^{-1}$ and $r_c = 1000 \text{ kpc}$) are over-plotted with red diamonds. Each panel has three dotted lines that show, from bottom to top, $\Delta\chi^2$ values above the minimum of 1, 4, and 9, corresponding to 1, 2, and 3 σ confidence intervals of each individual parameter. A heavy black line is drawn connecting the smallest χ^2 values for each parameter value. We have good constraints on black hole mass $M = 6 \times 10^8 M_\odot$ with 1, 2, and 3 σ uncertainty ranges of $5.1\text{--}6.7 \times 10^8$, $3.2\text{--}8.9 \times 10^8$, and $1.4\text{--}12 \times 10^8 M_\odot$, respectively.

but simple circular stellar orbits could not reproduce all of the kinematic data (Fig. 5). Two potential explanations are that (1) the stellar orbits in the ring are non-circular or (2) a large fraction of the stars in the ring are counter-rotating. Non-circular orbits would increase the line-of-sight velocity and velocity dispersion as a function of radius for stars in a spherical potential that has the same enclosed mass profile as the non-spherical potential of NGC 3706. The orbits considered were rosette orbits with apocenters and pericenters corresponding to the outer and inner extents of the stellar ring. These rosette orbits were able to reproduce the high observed velocity dispersion, but not the low observed $|V|/\sigma$. Thus, we

conclude that the stars in the stellar ring are orbiting in both senses.

If a significant fraction of the stars are counter-rotating, then the mean velocity of stars at a given radius would tend closer to zero and the dispersion would increase. This is the solution found by our best fitting model with approximately 1/3 of the stars in the ring counter-rotating. A partially counter-rotating ring sufficient to drop the line-of-sight $|V|/\sigma$ to the observed ratio necessarily implies LOSVDs that are asymmetric about their mean in the ring. This asymmetry is seen in the data as can be ascertained from the high value of the third Gauss-Hermite moment of $h_3 = 0.09$ at $R = -0''.25$ and the only negative value at $R = +0''.25$ of $h_3 = -0.029$ (Table 1). The

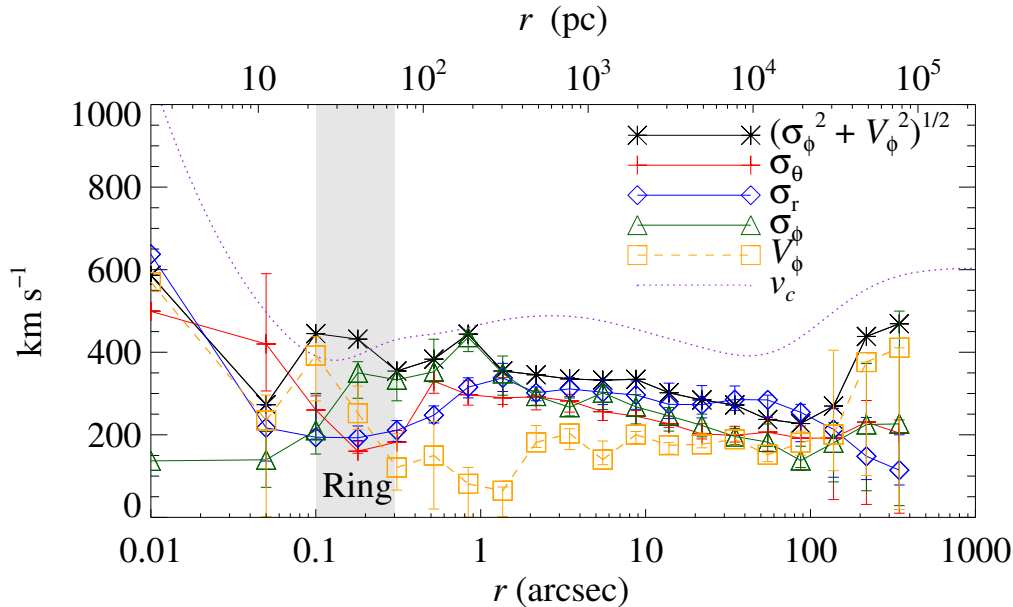


Figure 7. Kinematics of the best fitting orbit model in the equatorial plane. Each symbol shows the dispersion in the direction indicated by the legend, where r is the radial direction, ϕ is the tangential direction, and θ is the altitude angle (i.e., angle above the equatorial plane) direction. In the equatorial plane $\sigma_\theta = \sigma_z$. The error bars show the ranges of values derived from models within $\Delta\chi^2 < 4.7$ (1σ confidence for 4 parameters) of the minimum. The region roughly occupied by the stellar ring is shaded light gray. In the region of the ring, σ_θ and σ_r decrease markedly while σ_ϕ and $(\sigma_\phi^2 + V_\phi^2)^{1/2}$ are steady or increase within the ring region. The decrease in σ_θ and σ_r is as expected by a stellar ring. We also show the circular velocity calculated from the potential of the best-fitting model ($v_c^2 = r\nabla\Phi$).

LOSVD of the $R = -0''.25$ observational bin can be seen to be asymmetric in the right panel of Figure 8. This observed LOSVD is well matched by the best-fit model (black solid line in Fig. 8). The model LOSVD is composed mostly of (i) a bimodal distribution of circular and nearly circular orbits in both directions (red crosses), (ii) a unimodal distribution of more eccentric orbits that orbit in both directions (blue diamonds), and (iii) orbits of stars outside of the ring seen in projection at the location of the ring (brown \times symbols). The distinction between the first two categories is subtle and depends on whether the orbit is entirely in the region where the ring is highly visible, as it is for (i), or if, as it is for (ii), only the pericenters of the orbits peak into the ring while the apocenter is outside, in the region where the light of the ring blends into the background light of the galaxy. The orbit library in our best-fit model contains 31,804 orbits, of which 168 are type (i). Of those 168 orbits, 13 have non-negligible weights in our orbit reconstruction and make up the system in our models (Fig. 8, right panel, thick red line). Thus the solution found by the model includes a stellar ring with stars orbiting in both directions.

A potential concern is that since we can only observe projected velocity distribution along the line of sight, what appears to be a ring that has stars rotating in both directions could actually be a ring that rotates entirely in one direction but in the opposite sense of the rest of the galaxy. First, we note that a mono-counter-rotating ring can be calculated by our axisymmetric models but was not the best-fit solution. To directly address this concern, we performed a simple kinematic decomposition of the ring from the background galaxy (Fig. 9). Using only the STIS data, we took on-axis LOSVDs from the location of the ring and subtracted a weighted offset LOSVD at the same distance from the minor axis. This decomposition makes the reasonable assumption that the bulge LOSVD just off the major axis is similar to the bulge contribution to

the LOSVD on the major axis. The weight should be equal to the fraction of light in the on-axis bin that does not come from the ring. That is, it is foreground and background light due to the bulge of the galaxy. Based on extrapolation of the surface brightness profile, roughly 1/3 of the light could come from stars not in the ring. The resulting decomposed ring LOSVDs, however, still have a substantial component that rotates in the opposite sense to the rest of the ring (Fig. 9). Even if we assume that half of the light in the vicinity of the ring actually comes from foreground and background stars—and ignoring the unphysically negative values for the LOSVD that result—there is still a substantial counter-rotating component to the ring (i.e., stars with negative velocity in the left panel of Figure 7, and with positive velocity in the right panel). The effect is more pronounced at the ansae, (Fig. 9; $R = -0''.250$) where the differences in line-of-sight velocity of the counter-rotating components are maximized. So it is not possible to self-consistently model the ring data without a counter-rotating component.

We note that the kinematics of the central stellar feature, in particular the low $|V|/\sigma$, can be produced by an edge-on bar structure. The photometry, however, is inconsistent with a bar. Galaxy-scale bars tend to be brightest at the center with either an exponential or a slow, nearly constant decrease in surface brightness along the bar major axis (Elmegreen & Elmegreen 1985; Kent & Glauddell 1989; Sellwood & Wilkinson 1993); and nuclear bars, though less well cataloged, perhaps decrease very steeply (e.g., Alard 2001). The central local minimum in surface brightness is at odds with a filled-out bar structure and is more naturally explained by a ring.

4.3. Self-gravity and stability of the ring

Our analysis of the ring in NGC 3706 raises several questions about the stability and longevity of this system. We consider (i) the vertical self-gravity of the ring, (ii) the mis-

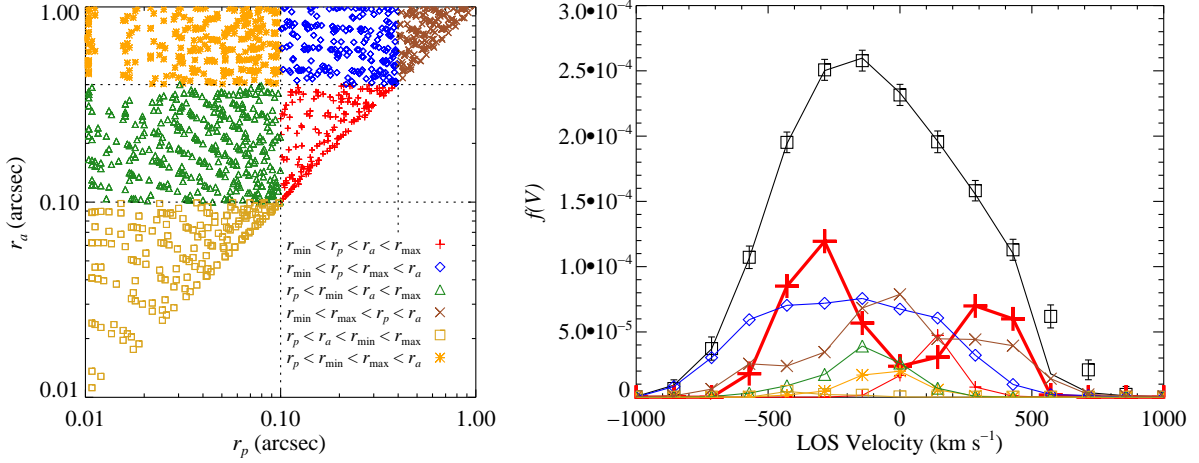


Figure 8. The left panel shows a portion of the pericenter-distance–apocenter-distance (r_p – r_a) plane and explains how we categorize orbits in the right panel depending on the relation of the orbits’ r_p and r_a compared to the ring minimum and maximum radii, $r_{\min} = 0''.1$ and $r_{\max} = 0''.4$, shown in dotted lines. Red + symbols are orbits that are entirely inside the ring’s radial extent. Blue \diamond symbols have r_p that lies within the ring’s radial extent but r_a that is external to the ring. Green \triangle symbols have r_a that lies within the ring’s radial extent but r_p that is internal to the ring. Brown \times symbols are entirely external to the ring. Goldenrod \square symbols are entirely interior to the ring. Finally orange * symbols have r_p interior to the ring and r_a exterior to the ring. The right panel plots the line-of-sight velocity distribution (LOSVD) of stars in the vicinity of the greatest extent of the stellar ring. The spatial extent is $0''.125 < r < 0''.375$ and $|z| < 0''.05$. The black \square symbols with error bars are the STIS data. The black line is the total best-fit model LOSVD and generally closely matches the observations except for underpredicting the number of large positive velocity orbits. The colored symbols with lines connecting them are contributions to the total model LOSVD from orbits as categorized in the left panel. LOSVD arising from orbits with $r_{\min} < r_p < r_a < r_{\max}$ (red + symbols) are plotted separately for orbits that are within the plane of the ring (thicker line) and for orbits that come out of the plane (thinner line). The total LOSVD (data and model) shows obvious asymmetric deviations from a pure Gaussian, as expected from consideration of its large third Gauss-Hermite moment, $h_3 = 0.09$. The low value of $|V|/\sigma$ could not be modeled by a sum of co-rotating circular orbits. The red + symbols show that the orbits entirely within the radial extent of the ring are bimodal in velocity distribution, and the blue \diamond symbols show that the orbits with r_p within most of the ring but r_a immediately outside of the ring have a broad, unimodal distribution with a significant fraction orbiting in the opposite sense of the median of distribution. Thus the best-fit model includes a ring with stars rotating in both senses.

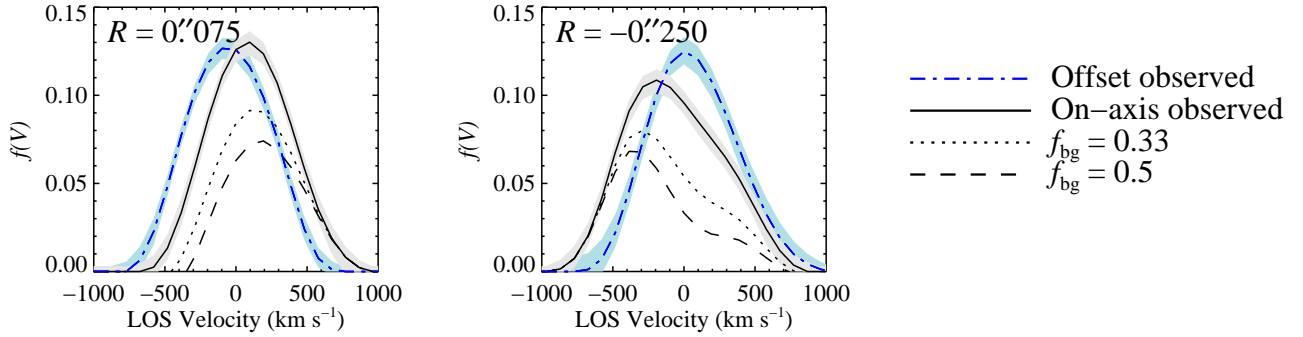


Figure 9. *HST*/STIS line-of-sight velocity distributions (LOSVDs) illustrating how the ring cannot rotate in one direction, counter to the sense of the rest of the galaxy. The left panel comes from cylindrical coordinate $R = 0''.075$, and the right panel comes from cylindrical coordinate $R = -0''.250$, where the negative indicates that it comes from the southeast side of the galaxy. These two were chosen because they had high signal-to-noise for both the on-axis and offset positions. In both panels, the observed LOSVDs are plotted as continuous curves with shaded regions indicating 1σ uncertainty regions. The two other curves are the on-axis LOSVD after subtracting the offset LOSVD, weighted by f_{bg} . Thus the dotted and dashed curves show the LOSVD of the ring only after a kinematic decomposition, assuming that the rest of the galaxy (other than the ring) makes up a fraction f_{bg} of the total light in the given bin. It can be seen that there is still substantial counter-rotation in just the decomposed ring LOSVD.

alignment of the ring with the bulge, and (iii) the stability of the counter-rotation. For ease of computation, in the remainder of this subsection we make a few simplifying assumptions about the bulge and ring. First, we assume that the axisymmetric spheroidal iso-density contours of the bulge have constant axis ratio $b/a = 0.68$ and have mass density at a semimajor axis a of

$$\rho(a) = \rho_0(a/a_0)^{-2} \quad (3)$$

where $\rho_0 = 480 M_\odot \text{pc}^{-3}$ and $a_0 = 50 \text{ pc}$. This form is an approximation² for the results from our photometric decomposition using our best-fit mass-to-light ratio, $Y_V = 6 M_\odot L_\odot^{-1}$. We assume the ring has constant surface density $\Sigma_0 = 6 \times 10^4 M_\odot \text{pc}^{-2}$ over its domain from $r = 20$ – 70 pc , giving a total ring mass of $M_r = 8.5 \times 10^8 M_\odot$. Although the vertical extent of the ring is unresolved, we assume that the mass density has

² The density is actually slightly shallower/steeper than a^{-2} inside/outside of 200 pc.

the functional form of an isothermal sheet:

$$\rho(z) = \frac{\Sigma_0}{4z_0} \operatorname{sech}^2\left(\frac{z}{2z_0}\right), \quad (4)$$

where the scale height, z_0 , must be small enough to remain unresolved. Note that the circular velocity at the radius of the ring is approximately constant at $v_c \approx 400 \text{ km s}^{-1}$.

4.3.1. Self-gravity of the ring

At the outer edge of the stellar ring ($r = 70 \text{ pc}$), the enclosed mass is made up of the black hole ($M = 6 \times 10^8 M_\odot$), the bulge stars ($M_b \approx 8 \times 10^8 M_\odot$), the dark matter halo ($M_{\text{DM}} = 3 \times 10^4 M_\odot$), and the ring itself ($M_r \approx 8.5 \times 10^8 M_\odot$). The ring's flatness raises the question of whether or not it is vertically self-gravitating, i.e., whether the vertical force is dominated by self gravity instead of gravitational forces from the black hole, bulge, and dark matter halo. We examine this question by considering the ring's Toomre (1964) Q parameter, which typically is $Q \sim 1$ for a vertically self-gravitating ring or disk embedded in a spherical stellar system that dominates the radial force.

Toomre's Q for stellar dynamical systems is given by

$$Q = \frac{\sigma_r \kappa}{3.36 G \Sigma_0}, \quad (5)$$

where κ is the epicyclic frequency. At the outer edge of the ring, the rotation curve is roughly flat (Fig. 4) so that $\kappa \approx 1.4\Omega = 1.4v_c/r = 2.6 \times 10^{-13} \text{ s}^{-1}$. Thus, $Q \approx 1.3$, and it is vertically self-gravitating.

4.3.2. Survival of a ring misaligned with the bulge

Because the ring is misaligned with respect to the symmetry plane of the axisymmetric bulge by an angle $i = 42^\circ$, the ring is subject to torques, which will cause the ring to precess, and dynamical friction, which can damp the misalignment.

The precession timescale of the misaligned ring is $\tau = (L \sin i)/N_{rb}$, where L is the total angular momentum of the ring and N_{rb} is the torque on the ring by the bulge. The total angular momentum of the ring about its rotation axis can be approximated by taking the entire ring to be at a radius $r_r = 50 \text{ pc}$ and rotating at a speed $v_\phi = 500 \text{ km s}^{-1}$ so that $L = \frac{1}{3} v_\phi r_r$, where the factor of $1/3$ comes from the fact that $\sim 1/3$ of the stars are counter rotating. The torque on a ring of mass M_r by the flattened bulge is

$$N_{rb} = \frac{5\pi}{2} G M_r \rho_0 a_0^2 \sin(2i) f(c) = M_r n_{br}, \quad (6)$$

where we have defined n_{br} for convenience below and $f(c)$ is a function of the flattening, written in terms of $c^2 \equiv (a^2/b^2) - 1$:

$$f(c) = \frac{3}{2} \frac{c - \arctan c}{c^3} - \frac{1}{2} \frac{\arctan c}{c}. \quad (7)$$

For $b/a = 0.68$, $f(c) \approx -0.08$. The precession timescale is then $\tau \approx 2 \times 10^6 \text{ yr}$.

The calculation above assumes that the ring is rigid, which is a reasonable approximation if the mutual gravitational torques between the ring elements are strong enough to enforce rigid precession. To estimate the accuracy of this approximation, we simplify by splitting the ring into an inner and outer ring with masses, $M_i = 2 \times 10^8 M_\odot$ and $M_o = 6.5 \times 10^8 M_\odot$, and

radii $r_i = 20 \text{ pc}$ and $r_o = 70 \text{ pc}$, respectively. The torque on each ring is then

$$N_{i,o} = M_{i,o} n_{rb} \quad (8)$$

so that the difference in bulge torques is

$$N_\Delta = N_o - N_i = (M_o - M_i) n_{rb}. \quad (9)$$

The mutual torque between the two rings when misaligned from each other by a small angle ψ is

$$N_{rr} = \frac{3}{8} \frac{G M_i M_o}{r_o} \frac{r_i^2}{r_o^2} \sin 2\psi. \quad (10)$$

Combining Eqs. (9) and (10) shows that the torques balance for $\psi \approx 1^\circ$, which represents the amount of warping required to maintain rigid precession; the smallness of the warp confirms that the approximation of rigid precession is accurate.

The ring–bulge system in NGC 3706 is analogous to misaligned or warped galactic disks in dark matter halos. Dynamical friction from the halo damps warps in galactic disks, causing them to align on very short timescales, $\tau < 10^8 \text{ yr}$ (Dubinski & Kuijken 1995; Nelson & Tremaine 1995). If the same principles apply, the dynamical friction timescales would be much shorter for the NGC 3706 ring, which has an orbital period of $\sim 10^6 \text{ yr}$. Thus the ring should settle quickly to the symmetry plane of the bulge, and either we are seeing it shortly after creation, or there is another process maintaining the misalignment.

The presence of counter-rotating stars may excite, rather than damp, the misalignment. Nelson & Tremaine (1995) found that galactic warps may be excited by halos but only if the galactic disk and halo are rotating in opposite senses. However, given that only about one third of the stars counter-rotate, it seems probable that the inclination will still damp faster than it would excite.

4.3.3. Stability of the counter-rotating stream

The presence of counter-rotating stars raises the possibility that the ring is subject to a two-stream instability. The physics of the two-stream instability is more subtle in gravitating systems than in electrostatic plasmas: in contrast to a homogeneous plasma, a homogeneous gravitating system is already unstable at wavelengths larger than the Jeans length, so a two-stream instability can only be said to be present if the system is less stable than it would have been if the relative velocity of the two streams were zero (and for Maxwellian streams the opposite is true; see Lynden-Bell 1967 and Araki 1987). Sellwood & Merritt (1994) investigated the stability of self-gravitating disks in which half the particles were counter-rotating. They found a variety of outcomes depending on the radial velocity dispersion, ranging from apparent stability, to buckling instability, to in-plane lopsided ($m = 1$) instabilities. The nature of instabilities in counter-rotating disks also changes in the Keplerian regime, where the gravitational potential is dominated by a central point mass: in this case counter-rotating stars are often unstable to a secular $m = 1$ instability that leads to a precessing lopsided disk (Touma & Sridhar 2012). The ring in NGC 3706 is in neither the radially self-gravitating nor the Keplerian regime since its estimated mass is similar to the mass of the black hole (see Section 4.4.1). There is no evidence of asymmetry in the ring, which indicates either that the ring is axisymmetric, or the $m = 1$ component of any distortion is small, or that there is an $m = 1$ component with symmetry axis along the line of sight. Given the complexity of the dynamics

of counter-rotating rings and the limited accuracy with which we can determine the velocity distribution of the ring stars, we can make no definitive statements about stability.

4.4. Speculation on the ring's formation

The presence of counter-rotating stars in the stellar ring is unexpected, though not without precedent (Section 4.5). Here we speculate on a number of potential ways in which such a system could have formed.

4.4.1. Multiple tidal disruptions

If the creation of the stellar ring is through dissipative accretion, as argued by Lauer et al. (2002), it would have to be through at least two accretion events. At the inferred mass-to-light ratio of $\Upsilon_V = 6 M_\odot L_{\odot,V}^{-1}$, the estimated mass of the ring is approximately $7.8 \times 10^8 M_\odot$, or approximately equal to the mass of the black hole. The stellar mass of the ring could be supplied by two dwarf galaxies or several tens of stellar clusters. If the coplanarity of the counter-rotating stars in the stellar ring is merely a chance alignment of independent disruption events, then it would be far more likely for it to happen with just two stellar systems, which would require the two accreted systems to be dwarf galaxies. The typical central stellar density of a dwarf galaxy is $\rho_* \sim 1 M_\odot \text{pc}^{-3}$. Assuming that tidal disruption of a stellar system by a black hole of mass M happens roughly at a distance

$$r_d \sim \left(\frac{3M}{4\pi\rho_*} \right)^{1/3}, \quad (11)$$

dwarf galaxies would be disrupted at distances of ~ 500 pc, much larger than the size of the ring (~ 20 – 75 pc). Thus, it would require subsequent dynamical evolution for the tidal debris to shrink to the observed size of the ring, which seems implausible. The typical central stellar density of a globular cluster, however, is $\rho_* \sim 10^4 M_\odot \text{pc}^{-3}$, corresponding to a tidal disruption distance of $r_d \sim 25$ pc, or about the size of the stellar ring. So tidal disruption of stellar clusters self-consistently explains the size of the ring but requires many such disruptions. The presence of older globular cluster stars could also explain the relatively redder color of the central $1''$ (Carollo & Danziger 1994). The chance superposition of several tens of globular cluster disruptions is so unlikely as to be precluded. If, however, there is a preferred plane in the potential of the galaxy, such as a large-scale disk, it could preferentially feed stellar clusters towards the central black hole on orbits with aligned or anti-aligned angular momenta. We note that this speculation is not supported by any evidence for a disk, and the misalignment of the ring with respect to the symmetry axis of the galaxy on larger scales makes this less likely.

4.4.2. Multiple gas accretion events

Another possible explanation is that the ring of stars formed in situ from gas accreted in two separate mergers. In such a scenario, the gas would funnel to the center of the galaxy and subsequently form a filled-in disk of stars as has been seen in other cases (e.g., Kormendy & Djorgovski 1989; Lauer et al. 1995; Kormendy et al. 2005). In order to form a counter-rotating structure, the first batch of accreted gas would have to form stars before gas from the second accretion event reached the nucleus. Note that this scenario is distinct from the scenario of bar-driven secular formation of a nuclear disk with

rings at the inner Linblad and ultraharmonic resonances of the tumbling triaxial potential seen in NGC 4750 (van den Bosch & Emsellem 1998). There is an established connection between bars and \sim kpc-scale nuclear rings (e.g., Buta & Combes 1996). There are cases where larger-scale nuclear rings are misaligned with respect to the bar structure (Buta et al. 1995), but it is not clear whether the observed misalignment between stellar ring and galaxy isophotes seen in NGC 3706 could occur at scales of ~ 10 – 100 pc. The observations present a number of constraints that can be used to determine qualitatively whether multiple gas accretion events can make the observed ring. The stellar ring has roughly the same mass as the central black hole, as has been seen in other nuclear disks thought to come from gas accretion events (Scorza & van den Bosch 1998). So the amount of mass we infer for the ring is reasonable for it to have come from gas accretion. A formation by multiple gaseous accretions would also predict a different color from the rest of the galaxy, as is observed. Note that the formation of the ring with multiple gas accretion events still requires either a preferential plane of the potential to funnel gas into the same planar orbit or else a coincidence in having the two accretion events come from the same plane with opposite rotational senses. This hypothesis is made more likely by the prevalence of nuclear disks in other early type galaxies.

4.4.3. Triaxial to axisymmetric potential

An interesting, though perhaps unlikely, way to make a counter-rotating disk is by having the initial disk in a triaxial potential that becomes axisymmetric. Box orbits in the triaxial potential become loop orbits in the axisymmetric potential in either prograde or retrograde directions (Evans & Collett 1994). If there is also a rotating azimuthal potential well, then there will be an asymmetry in the prograde–retrograde distribution of the resulting loop orbits as is seen in NGC 3706.

4.4.4. Resonant capture

Another mechanism for forming a counter-rotating disk is capture in the Binney (1981) resonance, where the rate of precession of the angular momentum vectors of the disk stars equals the pattern speed of some non-axisymmetric perturbation, for example the apsidal precession rate of a binary black hole. Stars captured in this resonance can be levitated from prograde to polar and then retrograde orbits if the pattern speed sweeps from negative to positive values (Tremaine & Yu 2000). The black hole binary could also have scattered away the inner regions of what was previously a filled-in disk to turn it into a ring. In all these scenarios, we are resorting to improbable events but this is to be expected since the NGC 3706 ring is unusual.

4.5. Comparison to other counter-rotating systems

NGC 3706 is not the first example of a counter-rotating stellar system, and here we mention some others. NGC 4550 is an S0 galaxy possessing a stellar disk with two spatially coexistent kinematic components (Rubin et al. 1992; Rubin 1994). Not only are the two kinematic components rotating in opposite directions from each other, but they have different stellar metallicities and ages, precluding a common origin (Johnston et al. 2012; Coccatto et al. 2012). At smaller scales, the cores of early-type galaxies also show evidence of distinct rotational components. Out of a sample of 260 early-type galaxies, as part of the ATLAS^{3D} project, Krajnović et al. (2011) identified

11 as having a kinematically distinct core, 8 as having counter-rotating cores, and 11 as having two off-center symmetric peaks in velocity dispersion, separated by at least $0.5R_e$. At scales comparable to the stellar ring in NGC 3706, there is an eccentric disk in M31 (Lauer et al. 1993), which appears to require a black hole to maintain the eccentricity (Tremaine 1995). Kazandjian & Touma (2012) argue from N -body simulations that the eccentric disk was created from counter-rotating stellar clusters, which is analogous to our hypothesized formation for the stellar ring in NGC 3706, though the stellar mass in the eccentric M31 disk is much smaller. At even smaller scales, within ~ 0.5 pc of the Galactic center, there appear to be two young stellar disks that rotate in different directions (Levin & Beloborodov 2003; Paumard et al. 2006; Lu et al. 2009; Bartko et al. 2009). More recently, Lyubenova et al. (2013) report the presence of counter-rotating orbits in the nuclear star cluster in FCC 277 based on high-spatial resolution IFU spectra and axisymmetric Schwarzschild modeling. There is, however, no direct analogy between the counter-rotating stellar ring in NGC 3706 and the above examples.

In the end, however unexpected, we have found it necessary to include a stellar ring with rotation in both directions in order to explain the observed $|V|/\sigma$ and LOSVD of the ring in NGC 3706. Based on our mass modeling, the ring is located at the tidal disruption radius of a stellar cluster for our black hole mass $M = (6_{-0.9}^{+0.7}) \times 10^8 M_\odot$. While this coincidence argues for a disruptive encounter between the progenitor of the stellar ring and the black hole, it requires many tens of dissipative encounters to make up the entire mass of the ring and some method for it to be aligned into a plane different from the galaxy's symmetry plane. Instead, it is probably more likely that two, unrelated, merger events led to the funneling of gas to the center of the galaxy and—after forming stars—resulted in a disk of stars, some of which are counter-rotating. A binary black hole could then scatter the inner stars, turning the disk into a ring, or even be responsible for the counter-rotation itself.

KG acknowledges support provided by the National Aeronautics and Space Administration through Chandra Award Number GO0-11151X issued by the Chandra X-ray Observatory Center, which is operated by the Smithsonian Astrophysical Observatory for and on behalf of the National Aeronautics Space Administration under contract NAS8-03060. This material is based upon work supported by the National Science Foundation under Grant No. AST-1107675. ST acknowledges support from NASA grant NNX11AF29G.

This research has made use of the NASA/IPAC Extragalactic Database (NED) which is operated by the Jet Propulsion Laboratory, California Institute of Technology, under contract with the National Aeronautics and Space Administration. This research has made use of NASA's Astrophysics Data System.

REFERENCES

- Alard, C. 2001, *A&A*, 379, L44
 Araki, S. 1987, *AJ*, 94, 99
 Bartko, H., Martins, F., Fritz, T. K., et al. 2009, *ApJ*, 697, 1741
 Binney, J. 1981, *MNRAS*, 196, 455
 Buta, R., & Combes, F. 1996, *Fund. Cosmic Phys.*, 17, 95
 Buta, R., Purcell, G. B., & Crocker, D. A. 1995, *AJ*, 110, 1588
 Carollo, C. M., & Danziger, I. J. 1994, *MNRAS*, 270, 523
 Coccato, L., Morelli, L., Pizzella, A., Corsini, E. M., Buson, L. M., & Dalla Bonta', E. 2012, preprint (1210.7807)
 Cretton, N., de Zeeuw, P. T., van der Marel, R. P., & Rix, H.-W. 1999, *ApJS*, 124, 383
 Dubinski, J., & Kuijken, K. 1995, *ApJ*, 442, 492
 Elmegreen, B. G., & Elmegreen, D. M. 1985, *ApJ*, 288, 438
 Evans, N. W., & Collett, J. L. 1994, *ApJ*, 420, L67
 Faber, S. M., & Jackson, R. E. 1976, *ApJ*, 204, 668
 Faber, S. M., Wegner, G., Burstein, D., Davies, R. L., Dressler, A., Lynden-Bell, D., & Terlevich, R. J. 1989, *ApJS*, 69, 763
 Ferrarese, L., & Merritt, D. 2000, *ApJ*, 539, L9
 Gebhardt, K., Adams, J., Richstone, D., Lauer, T. R., Faber, S. M., Gültekin, K., Murphy, J., & Tremaine, S. 2011, *ApJ*, 729, 119
 Gebhardt, K., & Thomas, J. 2009, *ApJ*, 700, 1690
 Gebhardt, K., Bender, R., Bower, G., et al. 2000a, *ApJ*, 539, L13
 Gebhardt, K., Richstone, D., Kormendy, J., et al. 2000b, *AJ*, 119, 1157
 Gebhardt, K., Richstone, D., Tremaine, S., et al. 2003, *ApJ*, 583, 92
 Goudfrooij, P., Hansen, L., Jorgensen, H. E., Norgaard-Nielsen, H. U., de Jong, T., & van den Hoek, L. B. 1994, *A&AS*, 104, 179
 Gültekin, K., Richstone, D. O., Gebhardt, K., Faber, S. M., Lauer, T. R., Bender, R., Kormendy, J., & Pinkney, J. 2011a, *ApJ*, 741, 38
 Gültekin, K., Tremaine, S., Loeb, A., & Richstone, D. O. 2011b, *ApJ*, 738, 17
 Gültekin, K., Richstone, D. O., Gebhardt, K., et al. 2009a, *ApJ*, 695, 1577
 ———, 2009b, *ApJ*, 698, 198
 Häring, N., & Rix, H.-W. 2004, *ApJ*, 604, L89
 Holley-Bockelmann, K., & Richstone, D. O. 2000, *ApJ*, 531, 232
 Johnston, E. J., Merrifield, M. R., Aragón-Salamanca, A., & Cappellari, M. 2012, *MNRAS*, 103
 Kazandjian, M. V., & Touma, J. R. 2012, preprint (1207.1108)
 Kent, S. M., & Glauddell, G. 1989, *AJ*, 98, 1588
 Kormendy, J. 1993, in *The Nearest Active Galaxies*, ed. J. Beckman, L. Colina, & H. Netzer (Madrid: Consejo Superior de Investigaciones Científicas), 197
 Kormendy, J., & Bender, R. 2013, *ApJ*, 769, L5
 Kormendy, J., Bender, R., & Cornell, M. E. 2011, *Nature*, 469, 374
 Kormendy, J., & Djorgovski, S. 1989, *ARA&A*, 27, 235
 Kormendy, J., & Gebhardt, K. 2001, in *American Institute of Physics Conference Series 586, 20th Texas Symposium on relativistic astrophysics*, ed. J. C. Wheeler & H. Martel (Melville, NY: AIP), 363
 Kormendy, J., Gebhardt, K., Fisher, D. B., Drory, N., Macchetto, F. D., & Sparks, W. B. 2005, *AJ*, 129, 2636
 Kormendy, J., & Ho, L. C. 2013, *ARA&A*, 51, 511
 Kormendy, J., & Richstone, D. 1995, *ARA&A*, 33, 581
 Krajnović, D., Emsellem, E., Cappellari, M., et al. 2011, *MNRAS*, 414, 2923
 Lang, M., Holley-Bockelmann, K., Bogdanovic, T., Amaro-Seoane, P., & Sesana, A. 2011, preprint (1107.2923)
 Lauer, T. R. 1999, *PASP*, 111, 227
 Lauer, T. R., Faber, S. M., Groth, E. J., et al. 1993, *AJ*, 106, 1436
 Lauer, T. R., Ajhar, E. A., Byun, Y., et al. 1995, *AJ*, 110, 2622
 Lauer, T. R., Tremaine, S., Ajhar, E. A., et al. 1996, *ApJ*, 471, L79
 Lauer, T. R., Gebhardt, K., Richstone, D., et al. 2002, *AJ*, 124, 1975
 Lauer, T. R., Faber, S. M., Gebhardt, K., et al. 2005a, *AJ*, 129, 2138
 ———, 2005b, *AJ*, 129, 2138
 Lauer, T. R., Gebhardt, K., Faber, S. M., et al. 2007, *ApJ*, 664, 226
 Levin, Y., & Beloborodov, A. M. 2003, *ApJ*, 590, L33
 Lu, J. R., Ghez, A. M., Hornstein, S. D., Morris, M. R., Becklin, E. E., & Matthews, K. 2009, *ApJ*, 690, 1463
 Lucy, L. B. 1974, *AJ*, 79, 745
 Lynden-Bell, D. 1967, *Cooperative Phenomena in Stellar Dynamics*, ed. J. Ehlers, 131
 Lyubenova, M., van den Bosch, R. C. E., Côté, P., et al. 2013, preprint (1303.1210)
 Magorrian, J., Tremaine, S., Richstone, D., et al. 1998, *AJ*, 115, 2285
 Malin, D. F., & Carter, D. 1980, *Nature*, 285, 643
 McConnell, N. J., & Ma, C.-P. 2013, *ApJ*, 764, 184
 McConnell, N. J., Ma, C.-P., Murphy, J. D., Gebhardt, K., Lauer, T. R., Graham, J. R., Wright, S. A., & Richstone, D. O. 2012, *ApJ*, 756, 179
 Murphy, J. D., Gebhardt, K., & Adams, J. J. 2011, *ApJ*, 729, 129
 Nelson, R. W., & Tremaine, S. 1995, *MNRAS*, 275, 897
 Paumard, T., Genzel, R., Martins, F., et al. 2006, *ApJ*, 643, 1011
 Pinkney, J., Gebhardt, K., Bender, R., et al. 2003, *ApJ*, 596, 903
 Quinn, P. J. 1984, *ApJ*, 279, 596
 Richardson, W. H. 1972, *Journal of the Optical Society of America* (1917-1983), 62, 55
 Richstone, D., Gebhardt, K., Aller, M., et al. 2004, preprint (arXiv:astro-ph/0403257)
 Richstone, D. O., & Tremaine, S. 1984, *ApJ*, 286, 27
 Rix, H.-W., de Zeeuw, P. T., Cretton, N., van der Marel, R. P., & Carollo, C. M. 1997, *ApJ*, 488, 702

- Rubin, V. C. 1994, *AJ*, 108, 456
Rubin, V. C., Graham, J. A., & Kenney, J. D. P. 1992, *ApJ*, 394, L9
Rusli, S. P., Thomas, J., Saglia, R. P., et al. 2013, preprint (1306.1124)
Sani, E., Marconi, A., Hunt, L. K., & Risaliti, G. 2011, *MNRAS*, 413, 1479
Schulze, A., & Gebhardt, K. 2011, *ApJ*, 729, 21
Schwarzschild, M. 1979, *ApJ*, 232, 236
Scorza, C., & Bender, R. 1995, *A&A*, 293, 20
Scorza, C., Bender, R., Winkelmann, C., Capaccioli, M., & Macchetto, D. F. 1998, *A&AS*, 131, 265
Scorza, C., & van den Bosch, F. C. 1998, *MNRAS*, 300, 469
Sellwood, J. A., & Merritt, D. 1994, *ApJ*, 425, 530
Sellwood, J. A., & Wilkinson, A. 1993, *Reports on Progress in Physics*, 56, 173
Siopis, C., Gebhardt, K., Lauer, T. R., et al. 2009, *ApJ*, 693, 946
Thomas, J., Saglia, R. P., Bender, R., Thomas, D., Gebhardt, K., Magorrian, J., Corsini, E. M., & Wegner, G. 2005, *MNRAS*, 360, 1355
Thomas, J., Saglia, R. P., Bender, R., Thomas, D., Gebhardt, K., Magorrian, J., & Richstone, D. 2004, *MNRAS*, 353, 391
Toomre, A. 1964, *ApJ*, 139, 1217
Touma, J. R., & Sridhar, S. 2012, *MNRAS*, 423, 2083
Tremaine, S. 1995, *AJ*, 110, 628
Tremaine, S., & Yu, Q. 2000, *MNRAS*, 319, 1
Tremaine, S., Gebhardt, K., Bender, R., et al. 2002, *ApJ*, 574, 740
Valluri, M., Merritt, D., & Emsellem, E. 2004, *ApJ*, 602, 66
van den Bosch, F. C., & Emsellem, E. 1998, *MNRAS*, 298, 267
van den Bosch, F. C., Ferrarese, L., Jaffe, W., Ford, H. C., & O'Connell, R. W. 1994, *AJ*, 108, 1579
van den Bosch, F. C., Jaffe, W., & van der Marel, R. P. 1998, *MNRAS*, 293, 343
van den Bosch, R. C. E., van de Ven, G., Verolme, E. K., Cappellari, M., & de Zeeuw, P. T. 2008, *MNRAS*, 385, 647